

# Effects of flexible wing on the aerodynamic performance of aircraft

Qinfeng Guo<sup>1</sup>, Zhuo Wang<sup>1</sup>, Jinjun Wang<sup>1\*</sup>

Fluid Mechanics Key Laboratory of Education Ministry, Beijing University of Aeronautics and Astronautics, Beijing 100191, China

\* jjwang@buaa.edu.cn

## Abstract

Wind tunnel experiments are conducted to investigate the effects of flexible wing on the aerodynamic performance of the simplified aircraft model with double membrane flexible wing and rigid wing. Aircraft aerodynamic forces as well as, membrane deformation and particle image velocimetry (PIV) at mid-span section are measured at Reynolds number of  $5.4 \times 10^4$ . The force measurement results show that both flexible and rigid wings encounter two-time stall. Compared with the rigid wing, the flexible wing presents a steeper lift curve in the linear regime. For the first stall, the delayed stall characteristics and the enhanced lift coefficient are obtained. When angle of attack is  $8^\circ$ , reattachment occurs after the separation caused by the blunt leading-edge for the flexible wing. Furthermore, the stronger mixing near the upper wing surface induced by the wing deformation suppresses the flow separation and improves the lift coefficient.

## 1 Introduction

Micro air vehicle (MAV) has shown great application and prospect in many fields due to its portability, high maneuverability and strong concealment since its emergence in 1990s. MAV belongs to a class of aircraft generally designated with a 15-cm maximum size dimension and capable of operating at 40-km/h maximum speed (Mueller 2001, Shyy et al. 2005). The MAV's Reynolds number of flight ranges between  $10^4$ - $10^5$ , at which the aircraft is in the unfavorable aerodynamic environment. Compared with rigid wing, flexible wing has better aerodynamic characteristics at low Reynolds numbers (Song et al. 2008, Béguin et al. 2010). Most of the early researches focused on the production of flexible wing, and MAVs with various configurations based on the carbon fiber skeleton and rubber membrane have achieved successful flights (Ifju et al. 2002, Lian et al. 2003, Shyy et al. 2005). In recent years, the biological membrane airfoil as well as the flexible wing aircraft has attracted much more attentions (Song et al. 2008, Béguin et al. 2012, Bleischwitz et al. 2018). Song et al. (2008) proposed a membrane airfoil based on the study of bats, and found that flexible wing has a strong hysteresis around the zero angle of attack as well as the stall angle. Hu et al. (2008) found that the membrane airfoil with free trailing edge can delay the stall angle of attack. Furthermore, the influence of gust and higher turbulence on stability can also be reduced. (Lian and Shyy 2007, Gordnier and Attar 2014).

It is confirmed that the flexible membrane could improve aerodynamics of wing and airfoil, and the mechanism is unclear. Taylor et al. (2005) studied the wing-tip deflection of the flexible delta wing,

they found that an increase in the level of buffet would indicate the existence of a lift enhancement region. By identifying the section deformation, Hu et al. (2008) found the free trailing edge deflection of membrane airfoil, which results in a reduction of the effective angle of attack, can delay the stall. Furthermore, the membrane deformation as well as vibration was found to be coherent with the vortex shedding, which influence the aerodynamic performance (Rojratsirikulz et al. 2009, Timpe et al. 2013, Bleischwiz et al. 2018).

To investigate the aerodynamic performance of the three dimensional flexible wing, Béguin et al. (2010) conducted a series of studies on a semi-span model with the double membrane morphing wing. According to the results of force measurement and flow visualization, better stall characteristics and higher aerodynamic efficiency have been achieved. Further research based on the membrane deformation measurement found that the membrane pre-strain, as well as the wing camber can be effectively altered by changing the wing configuration, which results in the relatively high lift-to-drag ratios over a broad range of flight conditions (Béguin et al. 2012). Based on the improvement of the baseline model, the pre-stress modification was achieved by moving the trailing edge spar (Béguin and Breitsamter 2014). Small pre-stress was found to lead to larger efficiency at low free-stream dynamic pressure and vice versa. Their present measurements, though, much more concentrated on the force and membrane deformation of the semi-span model, and the fluid structures are less involved.

In this paper, the simplified aircraft model with double membrane wing and rigid wing is designed. The force measurement is firstly conducted, followed by the PIV and deformation measurement carried out at the mid-span wing section of the upper wing surface. The second part of this paper mainly introduces the experimental setup. Then, the results of force measurement and fluid fields at angle of attack of  $8^\circ$  are discussed. Finally, a summary is provided.

## 2 Experimental Setup

The experiments were conducted in the open circulation low speed wind tunnel D1 at Beijing University of Aeronautics and Astronautics. As shown in figure 1a, the tunnel has a 1.45m-long oval test section with 1.02m×0.76m inlet and 1.07m×0.82m outlet. The maximum speed of wind tunnel is 40m/s, whereas the experiment speed is 20m/s.

As shown in figure 1b, the simplified aircraft model is designed, its fuselage has a total length of 219.3mm and a diameter of 40mm. The axial section of the nose is elliptic curve. For wing of the model, the leading edge sweep angle is  $15^\circ$ , the span is 269.7mm, and the length of wing root is 39.5mm. The experimental Reynolds number based on the length of wing root is  $5.4 \times 10^4$ . The flexible wing consists of a rigid leading edge and a telescopic trailing edge over which the Acrylonitrile Butadiene Styrene (ABS) flexible double membrane with thickness of 0.04mm is spanned. The membrane is attached to the rigid leading edge plainly when the sweep angle is  $15^\circ$ . At the trailing edge, the membrane is not attached to ensure the membrane deform smoothly. The rigid wing, which is made of the aluminum (LY12CZ) with thickness of 3mm, have the same planform configuration with the flexible wing.

For force measurement, the model was supported by a six-component strain balance, allowing recording of the time averaged force. The angle of attack was controlled by a mechanism with accuracy of  $0.05^\circ$ . The angle of attack varied from  $0^\circ$  to  $60^\circ$ , with the interval of  $1^\circ$  between  $0^\circ$  and  $20^\circ$  and the increment of  $2^\circ$  after  $20^\circ$ . The maximum blockage ratio was 2.2% obtained at the angle

of attack of  $60^\circ$ . The force measurement results were not modified because of the low blockage ratio, and the uncertainty is less than 3%.

The PIV measurement used the MicroPIV system, which employed a Nd:YAG double-plused laser as a light source with the power of 500mJ and wavelength of 532nm. Ethylene glycol droplets with diameter of  $1\mu\text{m}$  were employed as tracer particles. The resolution of the CCD camera was  $2456 \times 2058$  pixels to capture the area of about  $100 \times 80\text{mm}$  resulting in the magnification being  $0.04\text{mm}/\text{pixel}$ . The time interval between two straddle frames was  $20\mu\text{s}$ . To obtain the velocity fields, the multiple iterative Lucas-Kanade algorithm was used to process the raw practical images with the 75% overlap and final interrogation areas of  $32 \times 32$  pixels (Champagnat et al. 2011, Pan et al. 2015).

A high-speed Fastcam Photron SA2 CMOS camera was used to capture the upper wing surface deformation. The raw images had the resolution of  $2048 \times 2048$  pixels to cover the area of  $90 \times 90\text{mm}$ , which resulted in the  $0.04\text{mm}/\text{pixel}$  magnification. The membrane deformation was recognized by using a boundary recognition algorithm via gray scale threshold (Hu et al. 2019). For both PIV and deformation recognition, the measurement section was the mid-span location, and the distance between this section and wing root was  $57.4\text{mm}$ .

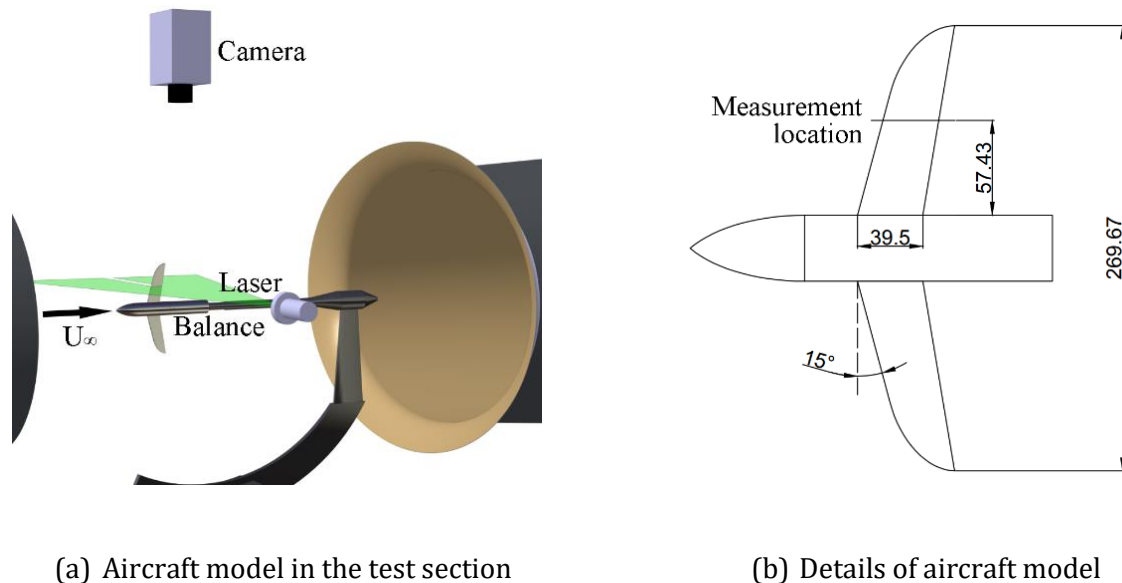


Figure 1. Experimental setup and test model

### 3 Result

Figure 2 shows the lift curves of flexible and rigid wings, that both have two-time stall. Two-time stall was not observed in the experiment of membrane airfoil, but coincide with the aerodynamic performance of swift wing (Zhan and Wang 2007). According to the variation of lift coefficient with angle of attack, it can be divided into four parts: linear regime, first stall, nonlinear regime, and second stall. For flexible wing, the linear regime refers to the part when the angle of attack is smaller than  $9^\circ$ , for the lift coefficient positively correlated with the angle of attack. When the angle of attack is between  $9^\circ$ - $16^\circ$ , the lift coefficient tends to decrease slightly, which is called the first stall. When

the angle of attack is in the range of  $16^\circ$ - $42^\circ$ , the lift coefficient rises again, but exhibits obvious nonlinearity, which is called the nonlinear regime. The maximum lift coefficient is achieved at angle of attack of  $42^\circ$ . Since then, the lift coefficient will decrease, called the second stall. Correspondingly, the  $0^\circ$ - $7^\circ$  of the rigid wing lift curve is called linear regime, the  $7^\circ$ - $8^\circ$  is called first stall, the  $8^\circ$ - $42^\circ$  is called the nonlinear regime, and the angle of attack larger than  $42^\circ$  is called the second stall.

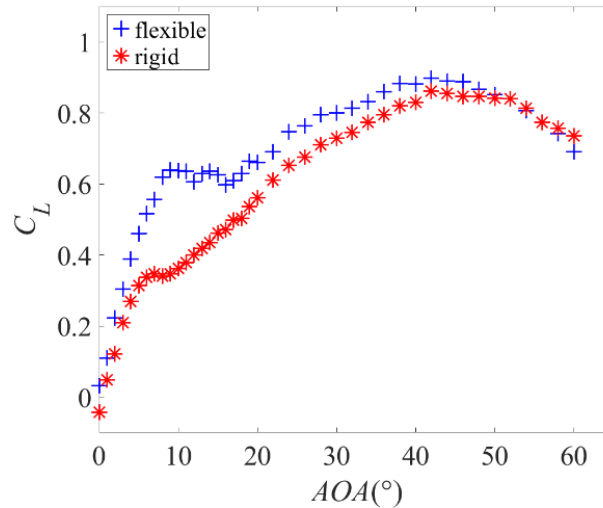


Figure 2: Lifts curve of flexible and rigid wings

The slope of flexible wing lift curve, which is obtained by using linear polynomial fit to the linear regime, is larger than that of rigid wing. For flexible wing, the slope is  $3.96\text{rad}^{-1}$ , whereas  $3.28\text{rad}^{-1}$  for rigid wing. Although the lift curves become generally nonlinear with the increment of angle of attack, this approximation still reflects the main trend of the linear regime.

The flexible wing shows smoother first stall characteristics with delayed stall angle of attack and increased first-stall lift coefficient. Compared with the rigid wing, the first stall angle for the flexible wing is delayed from  $7^\circ$  to  $9^\circ$ . Meanwhile, the corresponding lift coefficient is enhanced from 0.35 to 0.64 with the increment of 83.8%. For the second stall, the stall angles are same for the rigid and flexible wings, both being  $42^\circ$ . However, the maximum lift coefficient of the flexible wing is slightly larger than that of rigid wing with an increment of 4.2%.

When the angle of attack is  $8^\circ$ , the flexible wing approaches the first stall whereas the rigid wing is already in the first stall. At this angle of attack, the lift coefficient of flexible wing is 0.62 compared with 0.34 of rigid wing, resulting in an increment of 81.8%. For the mid-span location of the wing at this angle, the PIV experiment is conducted. The deformation of the upper flexible wing side is also identified.

Figure 3 shows the time averaged flow fields of flexible and rigid wings with the freestream normalized velocity magnitude  $u_{mean}/U_\infty$ , streamlines, and vorticity  $\omega c_{root}/U_\infty$  at the angle of attack of  $8^\circ$ . As presented in figure 3(a), the red lines show the time averaged deformation of wing upper side. The suction force on the upper side of flexible wing deflects the membrane upward, resulting in the increment of upper side camber. Streamlines show the different separation and reattachment processes near the upper side of the wing. For the flexible wing, the flow separation is caused by the blunt leading edge, after which, the reattachment occurs. It can be concluded that the flow is

dominated by the attached flow. For the rigid one, separated flow will not reattach downstream, and the whole surface is in the recirculation region. Time averaged velocity shows that high speed region of rigid wing is far from the upper surface of wing, while that of flexible wing is close to the upper surface and have larger value. Compared with the rigid wing, the maximum velocity  $u_{mean}/U_\infty$  of flexible wing is 1.44 with the increment of 13.9%. As shown in figure 3(b), the vorticity generates from the blunt leading edge for both flexible and rigid wings. But the shear layer of flexible wing is near the upper side of wing whereas the rigid wing shear layer is much more further. In addition, negative vorticity, induced by the trailing edge vortex of rigid wing, is observed.

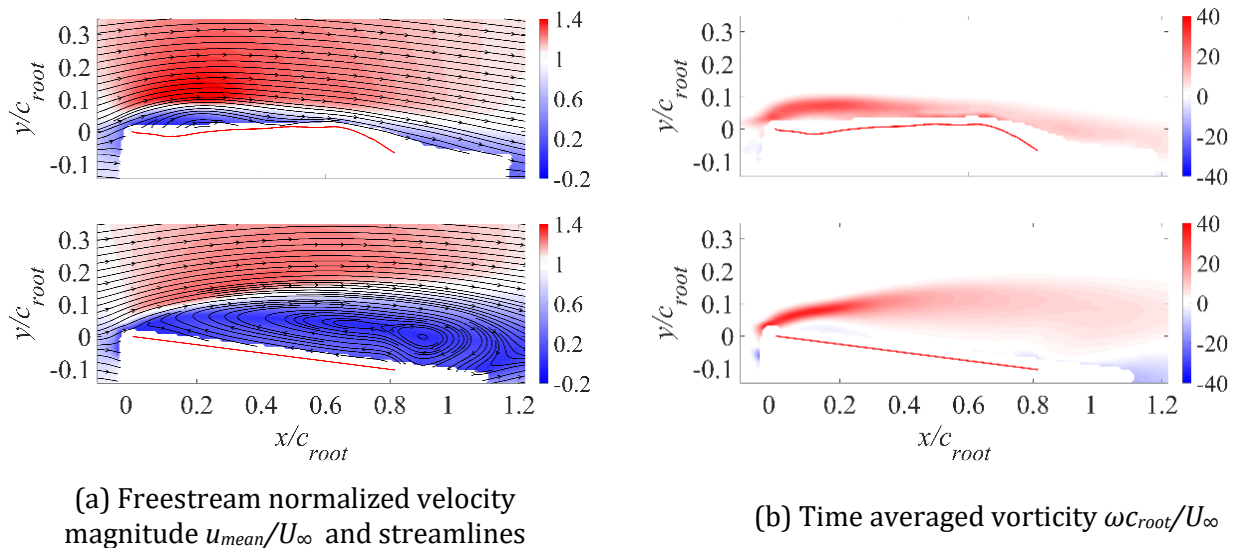


Figure 3: Time averaged flow fields of flexible wing (upper) and rigid wing (lower)

Figure 4 shows the  $u_{mean}/U_\infty$  distribution at  $x/c_{root}=0.2$  near the leading edge and  $x/c_{root}=1.5$  near the wake at angle of attack of  $8^\circ$ . As shown in figure 4(a), the flow recirculates near the rigid upper wing surface, while no negative value is observed for the flexible wing. The flexible wing deformation suppresses the separation of the leading edge and results in the increased velocity. In figure 4(b), the half-width of flexible wing wake is reduced by 25.1% accompanied with the reduced maximum velocity deficit. The half-width of the near wake region, determined by the vertical distance between the two points where the mean streamwise velocity falls to half of the maximum deficit (Shi and Feng 2015). In addition, the maximum deficit point of the flexible wing has a negative deviation, indicating that the increment of the camber is the cause of the larger lift coefficient.

Figure 5 shows the instantaneous distribution of vertical velocity fluctuations  $v'/U_\infty$ . The flow fluctuations of rigid wing appear to be generated by the leading edge separation of bluff body, and convect downstream accompanied with the leading edge vortex. For the flexible wing, the vertical velocity fluctuations are also generated by the leading edge. However, the flow fluctuations of flexible wing convect much closer to the upper side of wing due to the reattachment of the leading edge vortex and the dominated attached flow. Simultaneously, because of the flexible wing vertical vibration, the flow fluctuation near the upper side of wing are stronger than that of rigid wing.

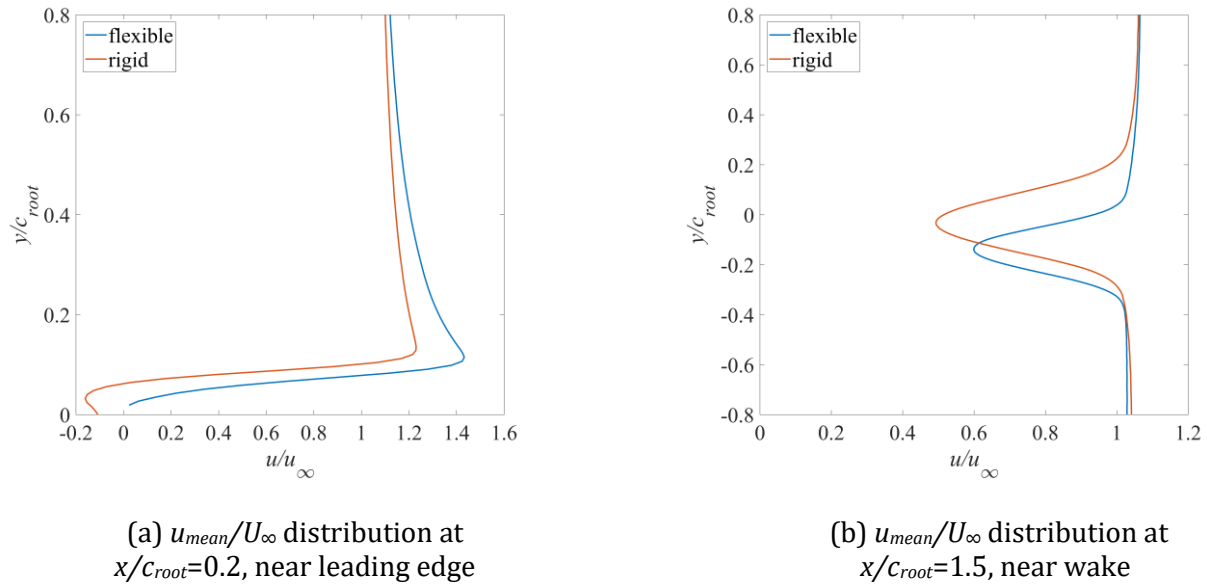


Figure 4:  $u_{mean}/U_{\infty}$  distribution at different streetwise locations

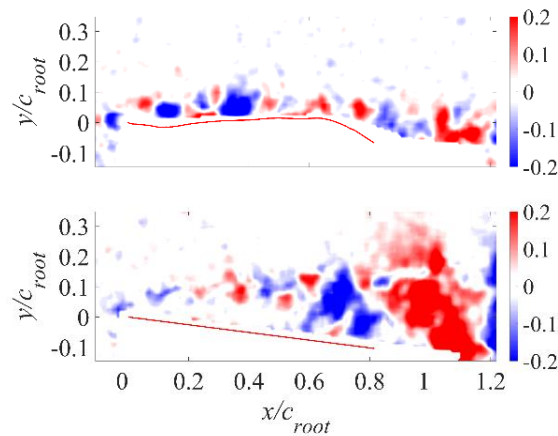


Figure 5: Instantaneous snapshot of vertical velocity fluctuations  $v'/U_{\infty}$  of flexible and rigid wing

To further analyze the fluctuation characteristics, Figure 6 shows the turbulence kinetic energy  $\overline{(u'^2 + v'^2)}/U_{\infty}^2$  and Reynolds shear stress  $-\overline{u'v'}/U_{\infty}^2$ . The turbulence kinetic energy in figure 6(a) highlights the regions of the disturbed flow. The rigid wing generates higher turbulence kinetic energy near the trailing edge. In comparison, flexible wing exhibits higher turbulence kinetic energy near the upper wing surface, which is coincide with the results obtained from the figure 5. In figure 6(b), the Reynolds shear stress is positive near the leading edge caused by the leading edge vortex, and then becomes negative for both rigid and flexible wings. The flow separation mainly causes the Reynolds shear stress of the rigid wing. For the flexible wing, membrane deformation causes stronger vertical fluctuations, and the Reynolds shear stress is concentrated near the upper side. The higher Reynolds shear stress near the upper side indicates the stronger flow mixing that suppresses the flow separation.

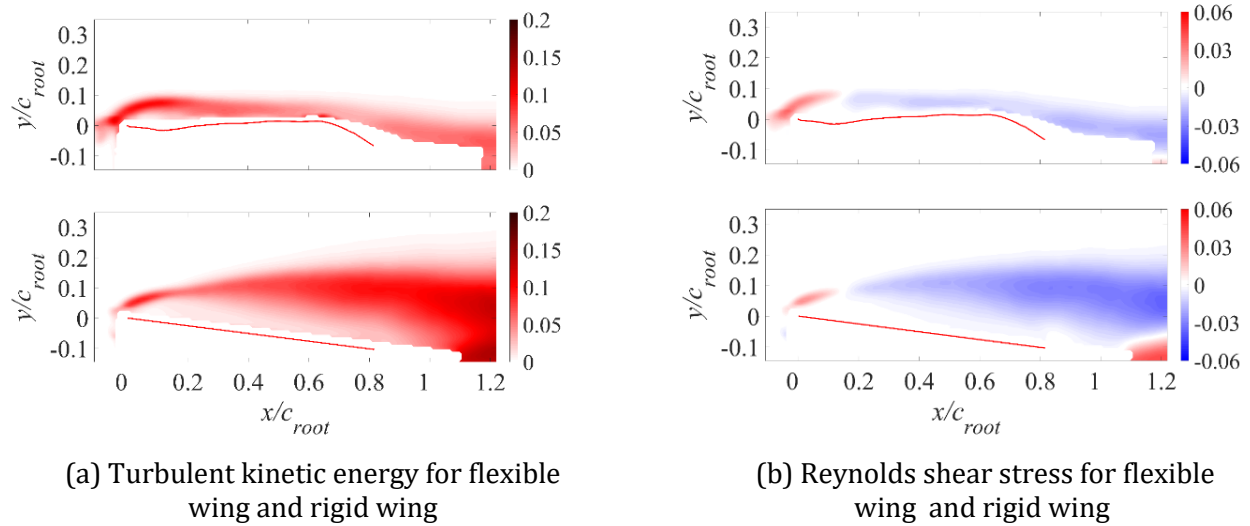


Figure 6: Turbulent kinetic energy  $\overline{(u'^2 + v'^2)}/U_\infty^2$  and Reynolds shear stress  $-\overline{u'v'}/U_\infty^2$

## 4 Conclusion

This paper studied the aerodynamic characteristics of the simplified aircraft model with double membrane flexible wing and rigid wing at Reynolds number of  $5.4 \times 10^4$ . The force measurement was conducted. Furthermore, the upper wing surface deformation and the flow fields were captured at mid-span section at angle of attack of  $8^\circ$ , at which the lift coefficient was obviously increased.

The lift curve showed that flexible wing had two-time stall, which was not observed in the experiments of membrane airfoil. According to the two-time stall, the lift curve could be divided into four parts including linear regime, first stall, nonlinear regime, and second stall.

In the linear regime, the lift curve of flexible wing was steeper than that of rigid wing. For the beginning of first stall, the angle of attack and lift coefficient of flexible wing were both larger than that of rigid wing. Especially, the lift coefficient was enhanced from 0.35 to 0.64 with an increment of 83.8%. For the maximum lift coefficient, that of flexible wing was increased by 4.2%.

Furthermore, upper wing surface deformation induced the reattachment, which occurred after the blunt leading edge separation of the flexible wing at angle of attack of  $8^\circ$ . Meanwhile, influenced by the stronger fluctuations, the separation of leading edge was also suppressed by the enhanced mixing near the upper side of flexible wing. Hence, higher lift coefficient was achieved.

## Acknowledgements

This work was supported by the National Natural Science Foundation of China (No. 11761131009 and 11721202).

## References

Béguin B, Breitsamter C, and Adams NA (2010) Experimental investigations of an elasto-flexible morphing wing concept. In *27th International Congress of the Aeronautical Science, Nice, France, September 19-24*

- Béguin B, Breitsamter C, and Adams NA (2012) Aerodynamic investigations of a morphing membrane wing. *AIAA Journal* 50(11):2588-2599
- Béguin B, and Breitsamter C (2014) Effects of membrane pre-stress on the aerodynamic characteristics of an elasto-flexible morphing wing. *Aerospace Science and Technology* 37:138-150
- Bleischwitz R, de Kat R, and Ganapathisubramani B (2018) Near-wake characteristics of rigid and membrane wings in ground effect. *Journal of Fluids and Structures* 80(1):199-216
- Champagnat F, Plyer A, Le BG, Leclaire B, Davoust S, and Le SY (2011) Fast and accurate PIV computation using highly parallel iterative correlation maximization. *Experiments in Fluids* 50(4):1169-1182
- Gordnier RE, and Attar PJ (2014) Impact of flexibility on the aerodynamics of an aspect ratio two membrane wing. *Journal of Fluids and Structures* 45:138-152
- Hu H, Tamai M, and Murphy JT (2008) Flexible-membrane airfoils at low Reynolds numbers. *Journal of Aircraft* 45(5):1767-1778
- Hu YW, Wang JS, Wang JJ, and Breitsamter C (2019) Flow-structure interaction of an inverted flag in a water tunnel. *Science China Physics, Mechanics & Astronomy* 62(12):124711
- Ifju P, Jenkins D, Ettinger S, Lian Y, Shyy W, and Waszak M (2002) Flexible-wing-based micro air vehicles. In *40th AIAA Aerospace Sciences Meeting, Reno NV, USA, January 14-17*
- Lian Y, Shyy W, Viieru D, and Zhang B (2003) Membrane wing aerodynamics for micro air vehicles. *Progress in Aerospace Sciences*. 39:425-465
- Lian Y, and Shyy W (2007) Laminar-turbulent transition of a low Reynolds number rigid or flexible airfoil. *AIAA Journal* 45(7):1501-1513
- Mueller TJ (2001) *Fixed and Flapping Wing Aerodynamics for Micro Air Vehicle Applications*. Chapter 1 An Overview of Micro Air Vehicle Aerodynamics. page 1-9. AIAA
- Pan C, Xue D, Xu Y, Wang JJ, and Wei RJ (2015) Evaluating the accuracy performance of Lucas-Kanade algorithm in the circumstance of PIV application. *Science China Physics, Mechanics & Astronomy* 58(10):1-16
- Rojratsirikul P, Wang Z, and Gursul I (2009) Unsteady fluid-structure interactions of membrane airfoils at low Reynolds numbers. *Experiments in Fluids* 46(5):859-872
- Shi XD, and Feng LH (2015) Control of flow around a circular cylinder by bleed near the separation points. *Experiments in Fluids* 56(12):214
- Shyy W, Ifju P, and Viieru D (2005) Membrane wing-based micro air vehicles. *Applied Mechanics Reviews* 58(4):283-301
- Song A, Tian X, Israeli E, Galvao R, Bishop K, Swartz S, and Breuer K (2008) Aeromechanics of membrane wings with implications for animal flight. *AIAA Journal* 46(8):2096-2106
- Timpe A, Zhang Z, Hubner J, and Ukeiley L (2013) Passive flow control by membrane wings for aerodynamic benefit. *Experiments in Fluids* 54(3):1471

13th International Symposium on Particle Image Velocimetry – ISPIV 2019  
Munich, Germany, July 22-24, 2019

Taylor G, Kroker A, and Gursul I (2005) Passive flow control over flexible non-slender delta wings.  
In *43rd AIAA Aerospace Sciences Meeting and Exhibit, Nevada, USA, January 10-13*

Zhan JX, and Wang JJ (2007) Experimental investigation on the longitudinal aerodynamic performance of common swift's wing. In *5th International Conference on Fluid Mechanics, Shanghai, China, August 15-19*